

EFFECTS OF PREHEATING ON X-RAY SCALING RELATIONS IN GALAXY CLUSTERS

JOHN J. BIALEK¹, AUGUST E. EVRARD^{1,2} & JOSEPH J. MOHR^{3,4,5}

ABSTRACT

The failure of purely gravitational models of X-ray cluster formation to reproduce basic observed properties of the local cluster population suggests the need for one or more additional physical processes operating on the intracluster medium (ICM). We present results from 84 moderate resolution gas dynamic simulations designed to systematically investigate the effects of preheating — an initially elevated ICM adiabat — on the resultant, local X-ray size–temperature, luminosity–temperature and ICM mass–temperature relations. Seven sets of twelve simulations are performed for a Λ CDM cosmology, each set characterized by a different initial entropy level S_i . The slopes of the observable relations steepen monotonically as S_i is increased. Observed slopes for all three relations are reproduced by models with $S_i \in 55 - 150 \text{ keV cm}^2$, levels that compare favorably to empirical determinations of core ICM entropy by Lloyd-Davies, Ponman & Cannon. The redshift evolution for the case of a locally successful model with $S_i = 106 \text{ keV cm}^2$ is presented. At temperatures $kT \gtrsim 3 \text{ keV}$, little or no evolution in physical isophotal sizes or bolometric luminosities is expected to $z \lesssim 1$. The ICM mass at fixed T is lower at higher z as expected in the canonical evolution model. ICM mass fractions show a mild T dependence. Clusters with $T \gtrsim 3 \text{ keV}$ contain ICM mass fractions depressed by modest amounts ($\lesssim 25\%$) below the cosmic mean baryon fraction Ω_b/Ω_m ; hot clusters subject to preheating remain good tracers of the cosmic mix of clustered mass components.

Subject headings: clusters: general — intergalactic medium — cosmology

1. INTRODUCTION

The hot, X-ray emitting plasma known as the intracluster medium (ICM) represents a part of the baryonic matter of the universe that isn't associated with individual galaxies but remains trapped in the deeper gravitational potential of galaxy clusters. Models of cluster formation in which the intergalactic gas simply falls into the dark matter-dominated gravitational well (so-called infall models) fail to reproduce all the structural properties of the local cluster population (*e.g.* Evrard & Henry 1991; Navarro, Frenk & White 1995; Mohr & Evrard 1997; Bryan & Norman 1998). There appears to be additional physics driving ICM evolution.

As early *ROSAT* and *Einstein* data emerged, several researchers proposed that the missing element is the existence of a high entropy intergalactic gas prior to a cluster's collapse (David et al. 1991; Evrard & Henry 1991; Kaiser 1991; White 1991). The resulting entropy floor breaks the self-similarity between the dark matter and ICM, because the equivalent thermal energy of the entropy floor corresponds to a larger fraction of the virial temperature in lower mass clusters.

A physical scenario consistent with this picture is one in which the bulk of star formation in a proto-cluster region occurs early in its formation history. Heating from supernova-driven galactic winds and AGN activity associated with the rapid star formation ultimately comes to exceed the cooling rate of ambient material, resulting in a period of net local heating. In the low-density limit, for

which subsequent cooling is unimportant, this feedback defines an initial adiabat S_i that is conserved in the absence of shocks. Later shock heating can raise the adiabat above this “entropy floor,” but the entropy cannot decrease below this level unless cooling becomes important.

Observational lines of evidence provide at least partial support for such a picture. Most of the stars in cluster elliptical galaxies are of a nearly uniform old age (Bower, Lucey & Ellis 1992; Kuntschner 2000, but see Trager et al 2000) and late-type galaxies within clusters are typically gas-poor and forming stars at a reduced rate compared to field galaxies (Cayette et al. 1994, Chamaroux, Balkowski & Gérard 1980). Even in MS1054, a very distant cluster at $z = 0.83$, much of the visible galaxy mass is contained in red, early-type galaxies (Van Dokkum et al. 1999). An active period of star formation in at least some regions of the $z \sim 3$ universe is inferred from the ultraluminous sources detected by SCUBA (Barger, Cowie & Richards 2000), and the population of Lyman-break galaxies, the distant equivalent of the local normal population, is forming stars at a rate substantially higher than today (*e.g.*, Steidel et al. 1999).

In addition to winds driven by star formation, the jets of radio galaxies present another potential source of ICM heating. *Chandra* observations of low emission measure bubbles in the ICM, aligned with the radio halos of central cluster sources (McNamara et al. 2000), implicate radio jets as another source of additional ICM entropy. The

¹Department of Physics, 1049 Randall Lab, University of Michigan, Ann Arbor, MI 48109

²Department of Astronomy, Dennison Building, University of Michigan, Ann Arbor, MI 48109

³Chandra Fellow

⁴Departments of Astronomy and Physics, University of Illinois, 1002 W. Green St, Urbana, IL 61801

⁵Department of Astronomy and Astrophysics, 5640 S Ellis Ave, University of Chicago, Chicago, IL, 60637

fact that the radio galaxies appear more frequently in clusters at higher redshift (Owen 2000) suggests that heating from this population might be more important in the past.

Of course, these and other observations also indicate that some late star formation and feedback does occur in cluster environments and this fact ultimately limits the accuracy and applicability of the approach used here.

A principal benefit of this approach is that the physical treatment of ICM evolution through gravitationally-driven shock heating is familiar territory for cosmological gas dynamic codes. Comparing the gravitational evolution of a single X-ray cluster derived from twelve nearly-independent codes, Frenk et al. (1999) find agreement in structural properties at characteristic levels of $\sim 5\%$ for dark matter and $\sim 10\%$ for the ICM.

The price for operating in a regime where the numerical accuracy has been calibrated is an approximate physical treatment. Neglect of radiative cooling is a particular concern, but the effect of radiative cooling and subsequent star formation on a cluster's thermal history is a complex problem. Observations indicate that ICM cooling occurs frequently in clusters, but the phenomenon is restricted to a core region containing $\sim 1\%$ of the collapsed (virial) cluster mass.

At early times, cooling is an important ingredient of the galaxy formation process (Rees & Ostriker 1977; White & Rees 1978). So important, in fact, that sources of heating must be introduced to stabilize its effects on small scales (White & Frenk 1991; Cole 1991; Blanchard, Valls-Gabaud & Mamon 1992). Attempts to model the full problem of the galaxy formation process within clusters are limited by poor knowledge of the correct parameterizations for star formation and feedback at arbitrary epochs. Semi-analytic methods (Kauffman, White & Guiderdoni 1993; Baugh, Cole & Frenk 1996; Wu, Fabian & Nulsen 1998, 1999; Somerville & Primack 1999) are best able to explore the large parameter space associated with these processes, but the lack of a direct solution for the spatial distribution of material limits the ability of this approach to predict detailed structural observables. Given current uncertainties, a scenario similar to our simple pre-heating assumption is not ruled out.

An initial entropy excess prevents gas from falling into the dark matter-dominated potential well to the extent it would in the purely gravitational infall model, thus reducing the central gas density. Core entropy¹ is related to temperature and density by $S_{core} \sim T/\rho_{core}^{2/3}$. If the temperature is set by the collisionless dark matter through the virial theorem $T \propto M_{200}^{2/3}$ (M_{200} is the mass encompassing a spherical density contrast of 200 with respect to the critical density), then the core density of initially preheated material will satisfy

$$\rho_{core} \lesssim M_{200} / S_i^{3/2}. \quad (1)$$

Higher levels of preheating will produce lower core densities and, for a given preheating amplitude S_i , low mass clusters will have less dense cores than high mass clusters. This differential effect results in a steepening of the slopes of the relations between density-dependent cluster observ-

ables (isophotal-size, luminosity and ICM mass) and temperature.

Previous simulations have found preheating to produce more realistic clusters in terms of the luminosity-temperature relation (*e.g.* Narvarro, Frenk & White 1995; Pierre, Bryan & Gastaud 1999). Metzler (1995) demonstrated a similar result using simulations that explicitly included the feedback of energy and mass from cluster galaxies. We seek here to systematically investigate preheating's effect on the size-temperature, luminosity-temperature, and ICM mass-temperature relations. Although not entirely independent observables, the functional dependence on the ICM density varies for these measures. Each probes a differently-weighted moment of the radial density profile. There is no guarantee, therefore, that a single preheating level S_i will provide a simultaneous match to all three relations.

We use a total of 84 moderate resolution numerical experiments consisting of twelve initial configurations run at six different levels of preheating plus a set evolved under infall for comparison. Since we lack a detailed mechanism for the preheating, all simulations are initiated with the gas held at a fixed, elevated temperature that corresponds to adiabatically evolved temperatures of a few million degrees at $z \simeq 3$.

In Section 2, the simulations are detailed. The effect of preheating on the major cluster relations are presented in Section 3. In Section 4, the range of entropies allowed by observation are determined and compared to other preheating studies. The effects on evolution, the virial mass-temperature relation, and gas fractions are explored in Section 5.

2. TECHNIQUES

2.1. The Simulations

The simulations are run using the Lagrangian code P3MSPH (Evrard 1988). The parameters of the models we employ are similar to that used for the P3MSPH contribution to the Santa Barbara cluster comparison study (Frenk et al. 1999). Initial conditions for our clusters are produced using the same multi-step procedure used in the Frenk et al. study. First, purely gravitational N-body runs are used to identify an ensemble of clusters for resimulation with gas dynamics. The final resimulation uses a combination of collisional and collisionless particles with a full gas dynamic treatment for a (Lagrangian) subset of the volume that comprises the cluster. An intermediate, low resolution N-body model is used to identify the Lagrangian region to be treated with gas dynamics.

The clusters are formed in a cold dark matter cosmology (Peebles 1982; Blumenthal et al. 1984) dominated by a non-zero cosmological constant, Λ CDM. The models assume a flat ($\Omega = 1$) geometry with the following parameters: $\Omega_m = 0.3$, $\Omega_\Lambda = 0.7$, $\Omega_b = 0.03$, $\sigma_8 = 1.0$, $\Gamma = 0.24$ and $h = 0.8$. The Hubble constant is defined as $100 h \text{ km s}^{-1} \text{ Mpc}^{-1}$; and σ_8 is the power spectrum normalization on $8h^{-1} \text{ Mpc}$ scales. Clusters form from initial density perturbations which are Gaussian random fields consistent with a CDM transfer function specified by

¹In this paper 'entropy', S , is expressed in units keV cm^2 according to the equation above. The usual thermodynamic definition of entropy is $s = c_V \ln(P/\rho^\gamma)$ where $\gamma = 5/3$ for a monotonic gas (appropriate for a fully ionized plasma). Using the equation of state for a perfect gas, $P = R \rho T$, the 'entropy' of this paper is related to traditional entropy by $S = e^{(s/c_V)}/R$.

$\Gamma \equiv \Omega h$ (Bond & Efstathiou 1984). Initial conditions are constructed using Zel’dovich’s formulation (*e.g.* Efstathiou et al. 1985).

The simulations begin with two 128^3 N-body runs which represent cubic regions 366 Mpc on a side from a CDM power spectrum. Clusters that form in this region have masses as large as $10^{15}M_{\odot}$ containing $\sim 10^3$ particles. We identify six clusters to resimulate from the final configurations of the two volumes: the two most massive clusters, a random pair less massive by a factor 3 from the mean of the first pair, and another random pair reduced in mass by a further factor 3. This results in a resimulated sample comprised of twelve clusters covering roughly a decade in mass.

The density field in cubic regions centered on the chosen clusters’ initial states are extracted from the original simulation and placed onto a higher resolution 64^3 grid. The size of the regions ranges from 50-100 Mpc and scales as the cube root of the mass enclosed within the turn around radius of the resimulated cluster. High frequency modes of the density field not sampled by the original simulation are then added, up to the new limiting Nyquist frequency. From this set of initial conditions the cluster is evolved in a purely N-body simulation of 32^3 particles, using alternate sampling of the 64^3 density field. Particles in this simulation that lie within a density contrast of 5 with respect to the background are used to define a Lagrangian mask. For the final gas dynamic resimulation, masked locations in the 32^3 subsampled field are expanded by a factor of two in resolution, generating an effective 64^3 resolution within the non-linear regions of the cluster. The high-resolution inner regions contain between 20,424 and 26,064 dark matter and gas particles in equal numbers. The inner regions are surrounded by 29,510 to 30,215 low-resolution dark matter particles that are each eight times the mass of a combined high-resolution gas and dark matter pair. This treatment allows the inclusion of both tidal effects from the surrounding large scale structure and the gas dynamics of the virial region in an economical way. The tidal particle contamination inside r_{200} at $z = 0$ is 0.0 – 0.1%. In addition, the cluster resimulations have mass resolutions which are similar fractions of the cluster virial masses despite spatial resolutions that range by a factor two, from 125-250 kpc.

Preheating is achieved by specifying an initial hot temperature for the baryons. The initial epoch is defined by a linear growth factor of 16 to the present day, resulting in an initial redshift $z_i = 20.82$ for Λ CDM. The initial temperature of the gas in the six preheating models ranges from $1.5 - 9.5 \times 10^7$ K compared to 10^4 K in infall models.

Table 1 lists the temperatures and corresponding initial entropies S_i for the seven models. The latter are derived using the cosmic mean baryon density at the initial epoch. Since the simulations have density perturbations at the outset, the entropy floor is not perfectly flat. Also listed in Table 1 are values of the gas temperature at $z=3$ that would place gas at the background density on the same initial adiabat. Energetically, at this epoch, the temperatures correspond to values between 0.07 and 0.4 keV per particle.

Table 2 lists basic properties of the complete set of 84 clusters at $z=0$. Groups are numbered by mass beginning with the highest mass group from each of the two initial

N-body models (labeled “a” and “b”). Individual runs are labeled by combining their model and group numbers with the initial entropy level (*e.g.* , a190S3).

TABLE 1
MODEL PROPERTIES

Model	S_i [keV cm ²]	$T_{adiab}(z=3.0)$ [K]	$T_i(z=20.82)$ [K]
S6	335.4	5.3×10^6	9.5×10^7
S5	221.8	3.4×10^6	6.0×10^7
S4	141.2	2.2×10^6	4.0×10^7
S3	105.9	1.7×10^6	3.0×10^7
S2	88.3	1.4×10^6	2.5×10^7
S1	53.0	8.4×10^5	1.5×10^7
S0	0.035	5.6×10^2	1.0×10^4

2.2. Data Processing

Mathiesen & Evrard (2001; hereafter ME01) find that there are significant differences (up to 20%) between the temperatures that theorists generally report and their observed counterparts. The values reported here build on the work of ME01 in order to be as close to observed values as possible. Luminosities and isophotal sizes are determined using the XSPEC `mekal` spectral emission model with 0.3 solar metallicity on a bandpass from 0.5 to 2.0 keV where the clusters are imaged at $z=0.06$. Unless otherwise stated, cluster temperatures used below are spectral values determined by the best fit of the cluster emission within r_{500} to an isothermal `mekal` spectrum in a 2.0 to 10.0 keV bandpass.

3. THE SCALING RELATIONS

Clusters exhibit a number of scaling relations that lend insight into their physical nature. A cluster’s X-ray isophotal size is tightly correlated with its emission weighted mean temperature; the so-called size-temperature relation (R_I-T ; Mohr & Evrard 1997; Mohr et al. 2000; hereafter M00). The relationship between a cluster’s luminosity and its temperature (L_X-T) has higher scatter, (David et al. 1993), reflecting its dependence on the ICM density distribution (the luminosity) and the total binding mass (temperature). This relation is important in determining the temperature function of a flux-limited sample of clusters. Because variations in ICM mass fraction are rather modest (Mohr, Mathiesen & Evrard 1999; hereafter MME99), the ICM mass correlates with cluster temperature leading to an $M_{ICM}-T$ relation. In addition to being useful in constraining cosmological parameters, these relations can be used to constrain models of the interaction between galaxies and the ICM.

3.1. Scaling Formalism

The self-similar model of Kaiser (1986) is a useful starting point in developing the expected behavior of the scaling relations to be considered in this section. The model assumes a smooth, spherically symmetric distribution of gas and total mass about its center. We follow notation similar to that of Arnaud & Evrard (1999). Let M_{Δ_c} be the total mass contained in a sphere (of radius r_{Δ_c} about the center) that encompasses a mean density $\Delta_c \rho_c$, where $\rho_c(z) \equiv 3H(z)^2/8\pi G$ is the critical density and $H(z)$ the Hubble parameter of the universe at epoch z . We write the ICM density $\rho_{ICM}(r)$ in terms of the natural radial

variable $y \equiv r/r_{\Delta_c}$

$$\rho_{ICM}(yr_{\Delta_c}) \equiv f_{ICM} \Delta_c \rho_c g(y) \quad (2)$$

where explicit use of the ICM mass fraction within a density contrast Δ_c

$$f_{ICM} \equiv \frac{M_{ICM}(< r_{\Delta_c})}{M_{\Delta_c}} \quad (3)$$

sets the normalization of the structure function $3 \int_0^1 dy y^2 g(y) = 1$.

A population of clusters that is strictly self-similar will have constant f_{ICM} and a single, specific function $g(y)$. Given the random and fully three-dimensional nature of cluster formation dynamics, strict self-similarity is an unrealistic expectation (Jing & Suto 1998; Thomas et al. 2000). A more reasonable expectation is that clusters are a *regular* population whose gas fraction values and structure functions will exhibit deviations depending, for example, on dynamical history. Searching for trends in the population with temperature, it is useful to employ mean gas fractions and structure functions

$$\hat{f}_{ICM}(T) \equiv \langle f_{ICM} \rangle_T, \quad (4)$$

$$\hat{g}(y|T) \equiv \langle g(y) \rangle_T \quad (5)$$

where $\langle \rangle_T$ denotes an ensemble average over clusters with temperature T .

Assume that the virial theorem holds, so that the mass M_{Δ_c} and temperature are linked by

$$M_{\Delta_c} = C_m T^{\alpha_m} \quad (6)$$

where the exponent α_m is 3/2 if spectral temperature is an unbiased measure of the mass-weighted value. Depending on the applied band pass, simulations display a bias that increases α_m by $\sim 10 - 20\%$ (Mathiesen & Evrard 2001; and see §5.2 below).

Finally, approximating cluster radial temperature profiles as isothermal, we can write the temperature scaling relations for M_{ICM} , L_X and R_I that are expected from a regular cluster population described by mean gas fractions $\hat{f}_{ICM}(T)$ and structure functions $\hat{g}(y|T)$. The ICM mass will scale as

$$M_{ICM} = C_m \hat{f}_{ICM}(T) T^{\alpha_m} \quad (7)$$

and the bolometric X-ray luminosity as

$$L_X = C_X \hat{f}_{ICM}(T)^2 Q_L(T) \tilde{\Lambda}(T) T^{\alpha_m}. \quad (8)$$

where $\tilde{\Lambda}(T)$ is a dimensionless emissivity (see Appendix) and $Q_L(T) \equiv 3 \int_0^1 dy y^2 \hat{g}^2(y|T)$. The size at fixed isophote requires an additional assumption about the projected radial profile of the emission. We assume a standard β -model for which $I(R) \propto R^{1-6\beta}$ outside the core. For this case, the expected scaling of isophotal size is

$$R_I = C_R [\hat{f}_{ICM}^2(T) Q_I(T) \tilde{\Lambda}(T) T^{2\alpha_m \beta}]^{1/(6\beta-1)} \quad (9)$$

with $Q_I(T) \equiv \int_0^{\sqrt{1-\xi^2}} d\eta h^2(\sqrt{\xi^2 + \eta^2})$ and $0.1 \gtrsim \xi^2 \lesssim 1$. For the typical value $\beta = 2/3$ (Jones & Forman 1984; MME99), this becomes

$$R_I = C_R \hat{f}_{ICM}^{2/3}(T) Q_I^{1/3}(T) \tilde{\Lambda}^{1/3}(T) T^{4\alpha_m/9}. \quad (10)$$

For self-similar clusters and mass-weighted temperatures, familiar scalings $M_{ICM} \propto T^{3/2}$ and $L_X \propto T^2$ emerge for the ICM mass and luminosity. The isophotal size in this case scales as $R_I \propto T^{2/3}$. Equations (7), (8) and (9) demonstrate that deviations of observed slopes from these expectations can arise from a number of sources. Temperature-dependent mean gas fractions and structure functions may be largely responsible, but metallicity trends that affect $\tilde{\Lambda}(T)$ and a virial slope $\alpha_m \neq 3/2$ will also tilt these relations.

3.2. The M_{ICM} - T Relation

Two-component β -model analysis of 45 clusters in the X-ray flux-limited Edge sample leads to an observed M_{ICM} - T relation of the form (MME99)

$$\log(M_{ICM}) = (1.98 \pm 0.18) \log(T_6) + (13.42 \pm 0.03) - \frac{5}{2} \log(h) \quad (11)$$

where M_{ICM} is the ICM mass within a density contrast of 500 in units of $h^{-1} M_\odot$ and $T_6 = T/6 \text{ keV}$. The slope 1.98 ± 0.18 is significantly different from the value of 3/2 expected from a strictly self-similar population.

Figure 1 displays the M_{ICM} - T relations at $\Delta_c = 500$ for the simulated cluster sets at zero redshift. In this and subsequent figures of this section, the temperature is the spectral fit to emission within r_{500} . This radius is chosen because it is observationally accessible, but our results are fairly insensitive to this choice. Slopes differ at the level of 0.6 – 6% between r_{500} and r_{200} . The dotted line in each panel is the MME99 observational result scaled to $h = 0.8$. Increased levels of preheating lead to steeper slopes in the M_{ICM} - T relation; the six preheated models sweep right through the observed slope.

For any given cluster, increasing the level of preheating progressively lower M_{ICM} . The entropy floor of the cluster effectively ‘plugs’, in the sense of making Jeans stable, some amount of core material. Later infalling matter encounters this material at progressively larger radii as S_i is increased, leading to spillover at larger radii. Lower mass clusters are affected by this to a larger degree because their virial adiabat is lower than that of rich clusters, eq. (1). The fit for each set of models is listed in Table 3. These fits are made only for clusters with $kT_s > 2.0 \text{ keV}$, to reflect the range over which the MME99 fit was made.

Models S1–S4 have slopes in statistical agreement with the observed value. The zero-points are higher than observed, which may be an indication that the global baryon fraction of 0.1 used in the simulations is $\sim 20\%$ too high. Care must be taken in making this comparison because the observed and simulated values scale differently with Hubble’s constant ($h^{-5/2}$ and h^{-1} , respectively). Re-scaling to $h = 0.7$ would raise the observed values 22% higher than the simulated measures, essentially eliminating the offset for model S3, for example. Since other factors like ICM clumpiness due to mergers (Mathiesen, Evrard & Mohr 1999) or a multiphase medium (Gunn & Thomas 1996; Nagai, Sulkanen & Evrard 2000) can affect the ICM mass at similar (10–20%) levels, we choose not to focus on arranging agreement in the zero-points of this and the other scaling relations. For any particular model, the global baryon fraction is tunable to arrange agreement in the ICM mass zero-point.

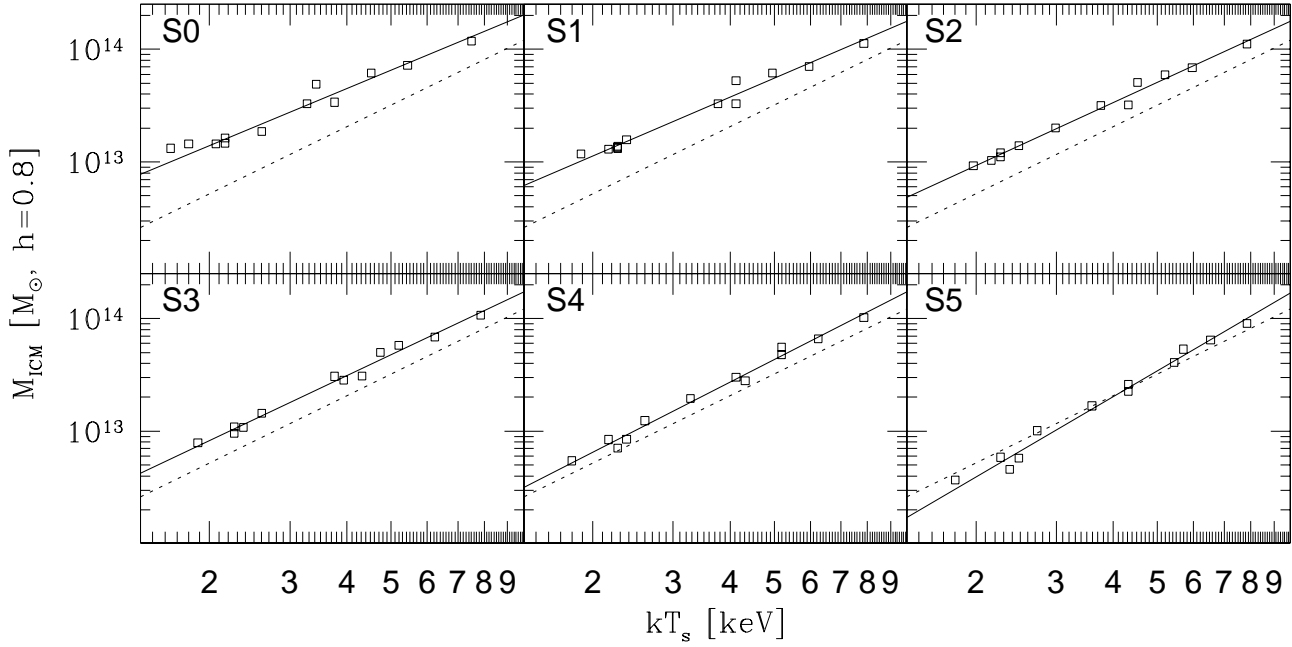


FIG. 1.— The ICM mass–temperature relation at $\Delta_c=500$ for 12 clusters run at 6 initial temperatures. The solid line is the best fit to clusters with $kT_s > 2$ keV. Dotted lines in each panel show the Mohr, Mathiesen, & Evrard observational result.

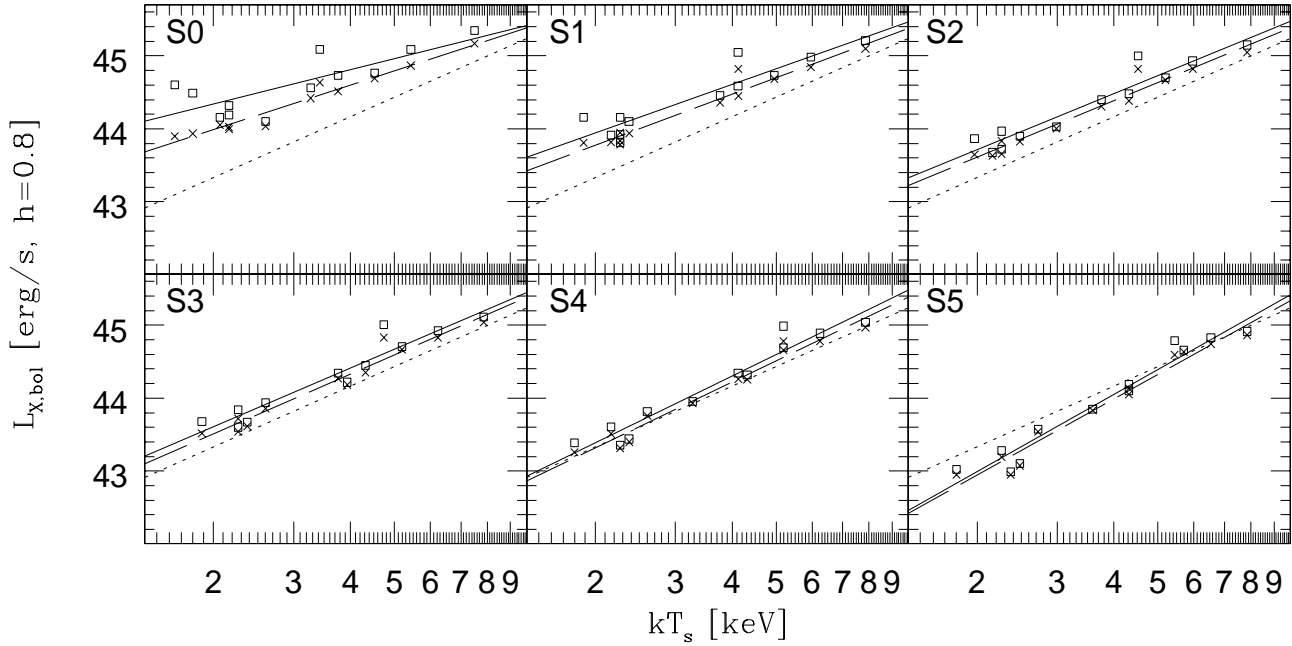


FIG. 2.— The final bolometric X-ray luminosity *vs.* spectral temperature for the 12 clusters evolved from 6 initial temperatures. Temperatures are estimated within r_{500} , luminosities are shown within r_{200} (open squares) or within that radius but with the core emission (within $0.13r_{200}$) removed (crosses). Solid and dashed lines are fits to these respective data. The observational result for $h=0.8$ is superimposed with a dotted line in each panel.

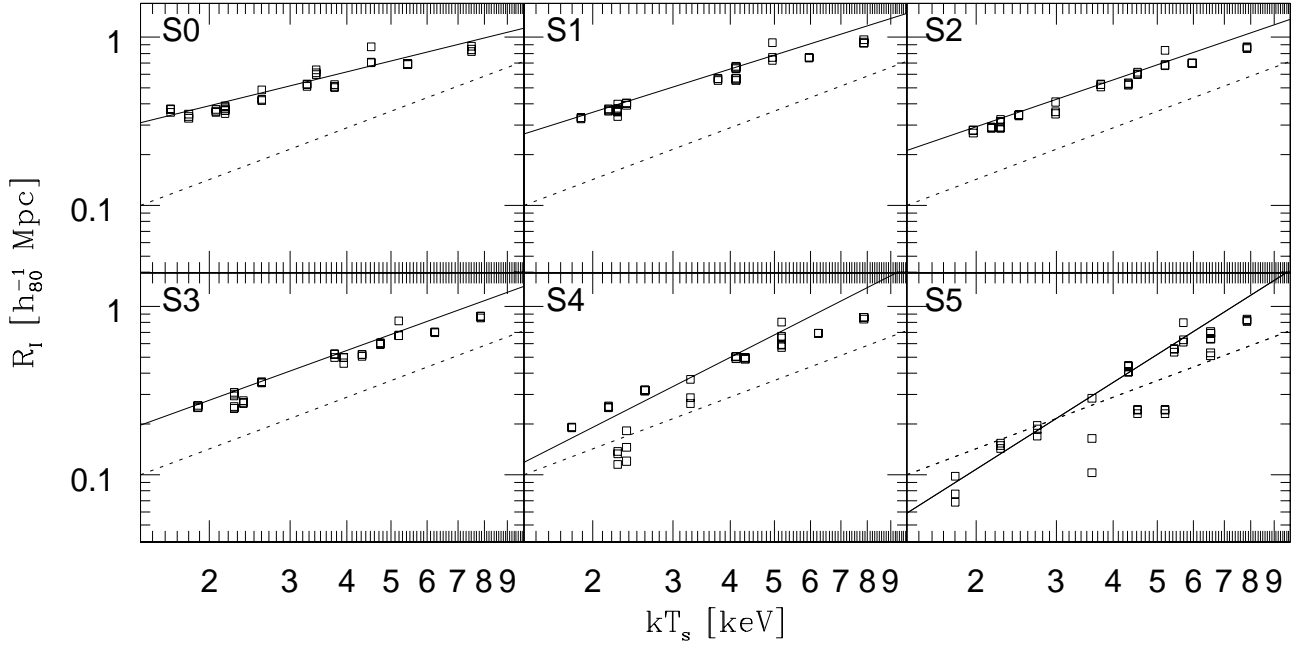


FIG. 3.— The size-temperature relations for the ensemble are shown for an isophote level $I = 10^3$ cts/s/arcmin². The solid line is the best fit to clusters with $kT_s > 2$ keV. The observed relation is represented by the dotted line.

TABLE 3
 FITS^a TO THE $M_{ICM}-T$, L_X-T & R_I-T RELATIONS AT $z = 0$ ($h = 0.8$)

Model	$M_{ICM}-T$		L_X-T (core - included)		L_X-T (core - extracted)		R_I-T	
	m	b	m	b	m	b	m	b
S6	2.67(0.13)	13.58(0.03)	3.96(0.26)	44.36(0.07)	3.95(0.24)	44.32(0.07)	4.05(0.39)	-0.04(0.05)
S5	2.37(0.10)	13.72(0.03)	3.52(0.25)	44.67(0.07)	3.47(0.21)	44.60(0.06)	1.72(0.15)	-0.15(0.02)
S4	2.07(0.08)	13.80(0.02)	3.03(0.24)	44.84(0.07)	3.00(0.18)	44.75(0.05)	1.38(0.18)	-0.06(0.04)
S3	1.92(0.08)	13.83(0.02)	2.67(0.25)	44.89(0.07)	2.71(0.19)	44.81(0.06)	0.98(0.07)	-0.09(0.02)
S2	1.86(0.07)	13.85(0.02)	2.55(0.24)	44.93(0.07)	2.57(0.17)	44.84(0.05)	0.93(0.05)	-0.09(0.02)
S1	1.73(0.09)	13.88(0.03)	2.20(0.28)	45.00(0.09)	2.32(0.18)	44.89(0.06)	0.85(0.07)	-0.04(0.03)
S0	1.69(0.12)	13.95(0.04)	1.56(0.38)	45.09(0.14)	2.02(0.13)	44.96(0.05)	0.67(0.06)	-0.09(0.02)
Observed	1.98(0.18)	13.66(0.03)	2.76(0.15)	44.67(0.03)			1.02(0.11)	-0.36(0.02)

^a Using the form $\log(X) = m \log(T_s/6 \text{ keV}) + b$.

3.3. The $L_X - T$ Relation

The $L_X - T$ relation has received considerable attention from observers (*e.g.* Edge & Stewart 1991; David et al. 1993) and computational model builders (Metzler 1995; Navarro, Frenk & White 1995; Allen & Fabian 1998; Eke, Navarro & Frenk 1998) over the last decade. An important contribution was made by Fabian et al. (1994), who showed that excess core emission associated with cooling flows is the primary source of the large scatter observed in the $L_X - T$ relation. The scatter is significantly reduced in analyses that either excise the core cooling flow regions (Markevitch 1998) or examine samples of clusters defined to possess weak cooling cores (Arnaud & Evrard 1999).

Since our simulations do not include the effects of cooling, we will compare them to the results of the studies that avoid cooling cores. Analyzing 26 clusters with accurate temperatures and inferred cooling rates $\dot{M} \leq 100 M_\odot \text{ yr}^{-1}$, Arnaud & Evrard (1999) find the correlation between bolometric luminosity and temperature $L \propto T^q$ with $q = 2.88 \pm 0.15$. Markevitch (1998) removes photons from the central $100 h^{-1} \text{ kpc}$ when calculating both the temperature and luminosity and this produces $q = 2.64 \pm 0.27$. We use an unweighted average of these two observational results, leading to a slope 2.76 ± 0.15 .

The bolometric $L_X - T$ relations for the model sets at a redshift of zero are displayed in Figure 2. Fits to each set to a relation of the form

$$\log(L_X) = (2.76 \pm 0.15) \log(T_6) + (44.48 \pm 0.03) - 2\log(h) \quad (12)$$

with L_X in units of erg s^{-1} are listed in Table 3.

Infall models (S0) exhibit a slope 1.44 ± 0.26 that is marginally inconsistent with the $L \propto T^2$ self-similar expectation (see Section 3.1). The slope is biased by the two lowest temperature systems; each lies a factor of roughly three above a fit performed under their exclusion. Examination of the pair's density profiles revealed that their core internal gas density profiles are steeper compared to the rest of the sample. A possible explanation of these enhancements is that they are transient effects of fortuitously observed mergers (Roettiger et al. 1996). Exclusion of core emission, where the core is defined as a circular area of radius $0.13r_{200}$ (Neumann & Arnaud 1999), yields a best fit $L_X - T$ slope 2.04 ± 0.16 , a value consistent with the analytic scaling. In Figure 2, crosses show the core-extracted $L_X - T$ relation and the dashed line shows the best fit.

Low-mass clusters, with lower virial entropy, feel the effects of preheating to a greater degree than high-mass clusters, resulting in a steepening $L_X - T$ relation as S_i is increased. The slopes of models S2-S4 are in agreement with observations. In the preheated models, no significant change in slope is seen by neglecting the core (see Table 3). The change in behavior compared to the S0 models is expected when one considers the fact that the core density is bounded from above by the imposed initial entropy, eq. (1).

The ability to match the $L_X - T$ slope is not unique to the instantaneous form of feedback assumed here. Metzler's (1995) models employing continuous energy feedback produce a slope of 2.96 ± 0.05 . The $L_X - T$ relation is also explained by semi-analytic models such as the shock model of Cavaliere, Menzi & Tozzi (1999) and models based on energy input and hydrostatic arguments (Wu, Fabian &

Nulsen 1998, 1999; Bower et al. 2000)

3.4. The $R_I - T$ Relation

The isophotal size R_I of a nearby cluster is tightly correlated to its temperature in a power law relation with slope near unity (Mohr et al. 2000, hereafter M00)

$$\log R_I = (1.02 \pm 0.11) \log(T_6) - (0.44 \pm 0.01) - \log(h) \quad (13)$$

with R_I in units of Mpc. Mohr & Evrard (1997) showed that the observed slope is steeper than the range $0.61 \leq m \leq 0.81$ found in sets of purely gravitational simulations of clusters in four different CDM cosmologies. The isophotal sizes from an ensemble of models experiencing continuous feedback showed a slope 0.99, consistent with observations.

Figure 3 illustrates the effect of preheating on the $R_I - T$ relation at zero redshift. The size R_I is determined at an isophote level $I = 3.0 \times 10^{-14} \text{ ergs/s/cm}^2/\text{arcmin}^2$. In each panel, an individual cluster contributes three data points, one for each orthogonal projection. Table 3 lists the best fit power law parameters for the simulations. Only clusters with $kT_s > 2 \text{ keV}$ are used in the fit, so as to match the range of the observed dataset used by M00. The fit is the average of 10,000 sets of 11 randomly drawn points. Assuming that 2 out of 3 projections can be treated as independent, each set excludes a random projection.

The slope of 0.67 ± 0.06 for the non-heated models (S0) is consistent with the scaling expected from eq. (9). This set has a mean value of $\beta = 0.825$ determined from fits to synthetic X-ray images, a value that leads to an expected $R_I - T$ relation slope of 0.63 by eq. 9. Preheating leads to steeper slopes; the six models produce a range of slopes that encompass the observed value. Model S3 is in best agreement with observation, and models S1 and S2 are marginally consistent.

The scatter about the $R_I - T$ relation is caused by effects of projecting the clusters along the line of sight, small equilibrium departures, and small ($\sim 5\%$) intrinsic fractional f_{ICM} variations due to variations in formation history. We defer analysis of variance until larger samples, both observational and computational, are available.

4. CONSTRAINING THE PREHEATING LEVEL

Preheating succeeds in reproducing the slopes of the three observed scaling relations considered in the preceding section. Figure 4 summarizes the results by displaying the slope fit to each of the preheated sets along with the observational constraints for the $M_{ICM} - T$, $L_X - T$ and $R_I - T$ relations. Simultaneous agreement in all three slopes can be satisfied within a range of initial entropy values near $\sim 100 \text{ keV cm}^2$. This is a non-trivial result that may signal preheating as a valid approximate treatment of at least the late-time evolution of the ICM.

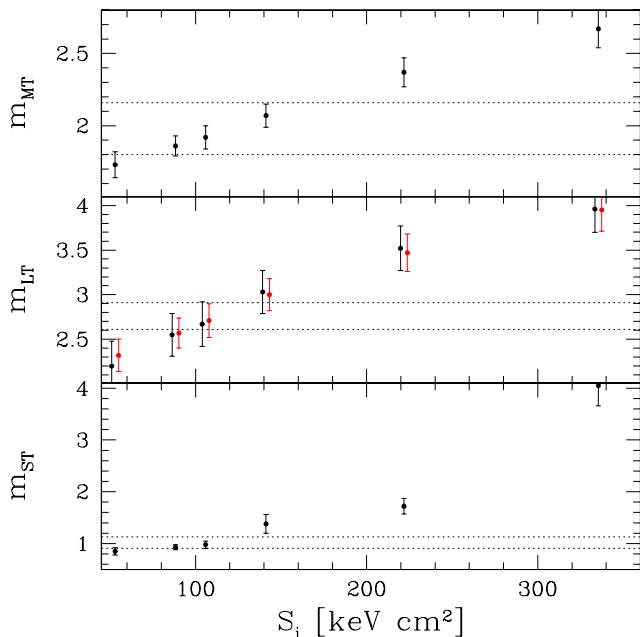


FIG. 4.— The $M_{ICM}-T$, L_X-T , and R_I-T slopes as a function of initial entropy. The allowed slopes based on observation are indicated by a pair of dotted lines. All errors are 1σ . The red symbols in the L_X-T panel represent the core-extracted fits (the two symbols have been offset about the S_i value for clarity).

We use a chi-squared measure based on the slopes of the three relations $\chi^2 = \sum_{i=1}^3 (m_{sim,i} - m_{obs,i})^2 / (\sigma_{sim,i}^2 + \sigma_{obs,i}^2)$ for each set of models in order to constrain the range of allowed preheating. Figure 5 shows the chi-squared for each relation individually and their sum. Horizontal lines indicate the 68.3%, 90% and 99% confidence limits for three degrees of freedom. From this analysis, the predicted level of preheating required to reproduce observation is between 55–150 keV cm² at 90% confidence.

This range overlaps with the one derived independently by Lloyd-Davies, Ponman & Cannon (2000). In an analysis of X-ray emission profiles of groups and clusters, they inferred a trend of decreasing central density with decreasing temperature, consistent with the constraint of a minimum central entropy in the range 34–82 keV cm² with 90% certainty. Pierre, Bryan, and Gastaud (1999) produced a suite of simulated clusters at a preheated entropy of 141 keV cm² and achieve results that are in agreement with the observed L_X-T relation (see also Pen 1999). Balogh, Babul & Patton claim success with a model in which the gas at the turnaround density is heated to 1.8×10^6 K at $z=1$, translating (for $\Omega_m=0.3$, $h=0.8$) into an equivalent entropy value 170 keV cm².

As previously mentioned, preheating is not unique in its ability to solve the L_X-T scaling relation problem. Semi-analytical models (Wu, Fabian and Nulson 1999a,b; Bower et al. 2000; Tozzi & Norman 2000) typically add energy into the ICM in a more gradual fashion. Since the evolutionary history of the ICM would differ in different scenarios, the behavior of the distant cluster population should decide between ICM histories based on rapid or more gradual heating. We turn next to predictions for ICM evolution at $z=0.5$ and $z=1$.

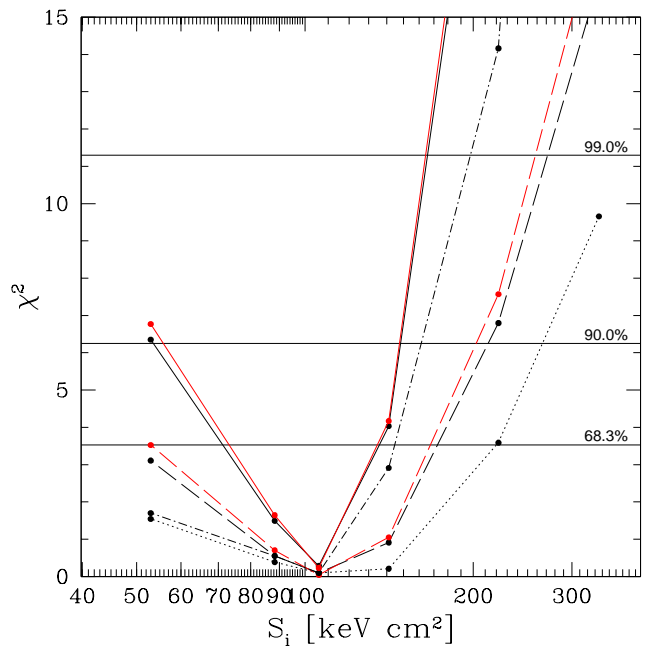


FIG. 5.— The χ^2 measure for the scaling relation slopes is shown as a function of initial entropy. The dotted, dashed, dot-dashed lines correspond to the $M_{ICM}-T$, L_X-T and R_I-T relations, respectively. The solid line indicates the χ^2 when considering all three relations. The red lines correspond to the use of the core-extracted L_X-T fits.

5. EVOLUTIONARY PREDICTIONS

Preheating affects the evolution of the ICM in a characteristic way. Observations of the distant cluster population can therefore be used to falsify the model or define the limits of its applicability. Figures 6 through 8 give a graphic representation of preheating's effect on cluster a1. The projected X-ray emissivity, thermal SZ signal, and emission-weighted temperature at redshifts 0, 0.5, 1 and 2 are shown for the same cluster under three treatments: no heating (model S0), a successful level of preheating (S3) and an excessively heated case (S6). The surface-brightness and temperature maps are made using the `mekal` emission model and the images are sized to be $2r_{200}$ on a side. The excessive model S6 shows the power of preheating to deplete the central ICM density of a cluster and severely limit its X-ray visibility at high redshift. The impact on the preferred model S3 is less dramatic. In this section, we present the redshift evolution of the locally successful set of S3 models only.

5.1. Evolution of Scaling Relations

Figures 9, 10 and 11 show evolution in the $M_{ICM}-T$, L_X-T and R_I-T relations, respectively, for model S3 at redshifts 0, 0.5 and 1. Table 4 provides fits to power law relations. The ICM mass and luminosity are measured within r_{200} at each redshift and the physical isophotal size is determined at a fixed intrinsic isophote level of $I = 3.0 \times 10^{-14}$ ergs/s/cm²/arcmin²

The simulations predict little evolution in the R_I-T and L_X-T relations to $z=0.5$. However, at $z=1.0$, both relations become $\sim 30\%$ steeper. Current observations of high redshift clusters appear consistent with these predictions. Mohr et al. (2000) find no significant evolution in their intermediate redshift study ($z \approx 0.2-0.5$) of CNOC clusters imaged by ROSAT. There is no significant evolution in

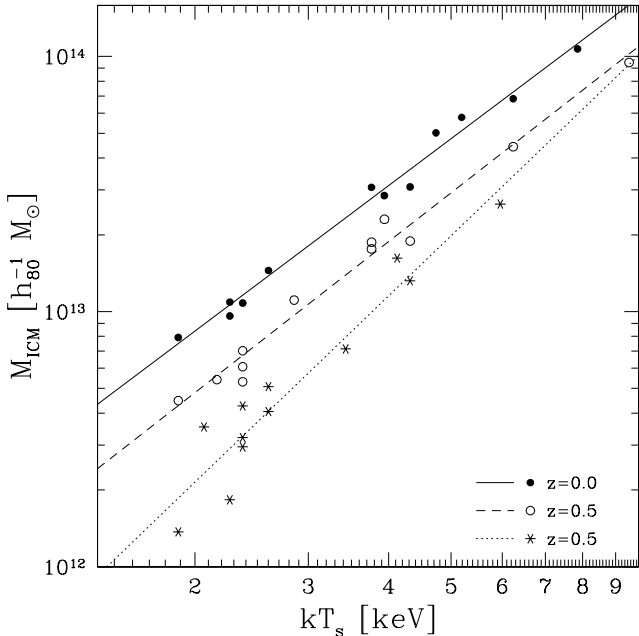


FIG. 9.— The ICM mass–temperature relation for 12 clusters of preheated model S3.

the L_X – T relation to redshifts ~ 0.5 (Mushotzky & Scharf 1997; Fairley et al. 2000). Higher quality data from the coming *Chandra* and XMM/Newton archives will tighten the constraints on the degree of allowed evolution.

Figure 9 illustrates that the M_{ICM} – T relation evolves toward lower ICM masses at higher redshift for fixed temperature clusters, as expected in the canonical evolution model. As with the R_I – T and L_X – T relations, no significant evolution in slope is expected at redshift 0.5 while a moderate steepening to $M_{ICM} \propto T_s^{2.4 \pm 0.2}$ is seen at $z = 1$. Because ICM masses within r_{200} require very deep imaging, less observational information is available for this relation at high redshifts. The expectations of model S3 appear consistent with observations (e.g., Matsumoto et al. 2000).

5.2. Virial Mass & ICM Mass Fractions

The fact that the M_{ICM} – T relation of set S3 is steeper than the canonical $3/2$ expectation arises from two separate factors. One is the relation between total mass and temperature and the other is the ICM mass fraction within r_{200} .

Non-preheated models follow a relation between total mass M_{Δ_c} and the mass-weighted temperature T_m that is consistent with expectations from the virial theorem $H(z)M_{\Delta_c} \propto T_m^{3/2}$ (e.g. Bryan & Norman 1998; M00; ME01). When a 2 – 10 keV spectral temperature is employed in place of the mass-weighted value, ME01 find that the relation steepens slightly to $H(z)M_{\Delta_c} \propto T_m^{1.6}$. Our non-preheated set of models (S0) is consistent with this steepening.

For the preheated set S3, Figure 12 presents the relation between total mass within r_{200} versus spectral temperature at $z = 0, 0.5$ and 1. Power-law fits to the data, listed in Table 5, indicate that slopes of 1.66 ± 0.12 and 1.73 ± 0.11 at $z = 0$ and 0.5, respectively, are consistent with the spectral relation of the non-preheated models. At

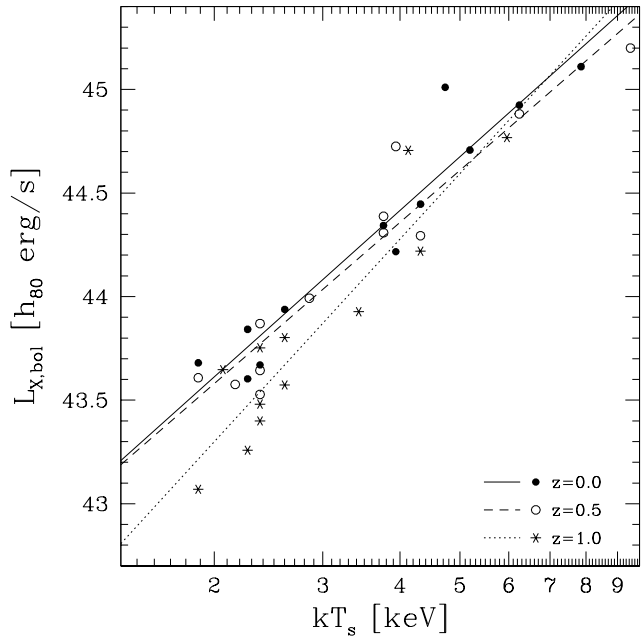


FIG. 10.— The luminosity–temperature evolution for the 12 clusters of the S3 model.

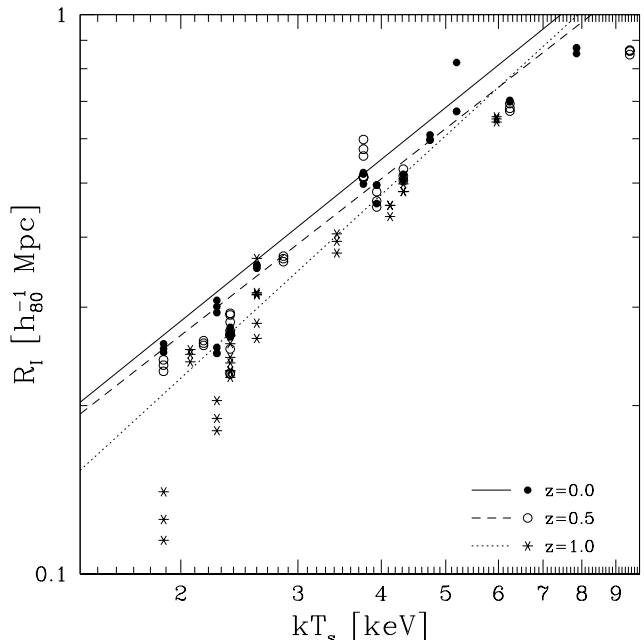


FIG. 11.— The size–temperature relation for model S3 at $z = 0, 0.5$ and 1.

$z = 1$, the slope steepens to 1.91 ± 0.11 . Note that the intercept at $T_s = 6$ keV remains stable, varying by only a few percent over the redshift range probed.

Observational determination of this relation can be attempted using weak lensing masses. Current data are too noisy to discriminate between a slope of 1.5 and 1.6 (Hjorth, Oukbir & Van Kampen 1999). Weak lensing masses are likely biased by the structures in which the clusters are embedded (Metzler et al. 1999); In addition to lensing masses, estimates based on galaxy kinematics (Horner, Mushotzky & Scharf 1999) or the hydrostatic assumption with measured temperature profiles are possible.

Nevalainen, Markevitch & Forman (2000) follow the latter approach for a sample of nine galaxies, groups and clusters and find a relation with slope 1.79 ± 0.14 , steeper by 2σ than the canonical 1.5 expectation but more in line with the relation from set S3. Finoguenov, Reiprich & Boehringer (2000) analyze a larger sample and find a slope of $1.78^{+0.10}_{-0.09}$, consistent with the Nevalainen et al (2000) results and inconsistent with self similar expectation at more than 3σ .

The ICM mass–temperature relations are steeper than that for the total mass at all redshifts for set S3, because the ICM mass fraction decreases at lower cluster temperatures. Figure 13 shows that the baryon fraction within r_{200} decreases from 9% at high temperatures to about 6% at 2 keV. Note that all values are consistently lower than the cosmic baryon fraction of 10%, an effect generally seen even in non-preheated simulations (MME99; Frenk et al. 1999). The fall-off at low temperatures is evidence of preheating’s stronger impact on shallower gravitational potentials.

Because cluster potentials tend to deepen with time, clusters evolve along this relationship toward values of higher ICM mass fraction.

Preheating and its effects on the ICM mass fraction and the $M_{ICM}-T$ relation is of direct relevance to the observability of high redshift clusters based on their X-ray emissivity or the thermal Sunyaev-Zel’dovich effect. The latter is particularly well suited for high redshift cluster detection. Using non-preheated simulations which with constant ICM mass fraction, Holder et al. (2000) show that proposed interferometric arrays would be capable of detecting clusters above a total mass limit of $10^{14} h^{-1} M_{\odot}$ at essentially any redshift. Haiman, Mohr & Holder (2000) emphasize the power of such surveys to constrain cosmological parameters Ω_M , Ω_{Λ} and the equation of the state parameter w of the dark energy component. An analysis of the effects of preheating on these yields an possible cosmological constraints in underway (Mohr et al. in prep.).

6. CONCLUSIONS

We have used a set of 84 moderate resolution gas dynamic simulations of cluster evolution to systematically investigate the effects of preheating on the local R_I-T , L_X-T and $M_{ICM}-T$ relations. We use a plasma emission model to estimate luminosities and determine spectral temperatures from fits to the overall cluster emission. We find that preheated models with initial entropy in the range $55 - 150 \text{ keV cm}^2$ reproduce the slopes of the observed scaling relations.

We have also compared these findings to the other preheating studies that have been conducted. There is good agreement between observation and simulations and our allowed range of entropies. Although this is a generous range, the new generation of X-ray satellites are sure to further constrain observations and narrow down the initial entropy found in clusters. Better understanding of this initial entropy aids in the deduction of ICM history and places restrictions on the mechanisms that are responsible for preheating.

Our examination of evolutionary effects is in agreement with the observed lack of evolution in all three relations at $z < 1.0$. However, we do find evidence for modest steep-

ening

TABLE 5
FITS TO $h(z)M_{200}$ vs. SPECTRAL TEMPERATURE FOR SET S3

z	m	b
0.0	1.66(0.12)	14.98(0.04)
0.5	1.73(0.11)	14.95(0.04)
1.0	1.91(0.11)	14.96(0.04)

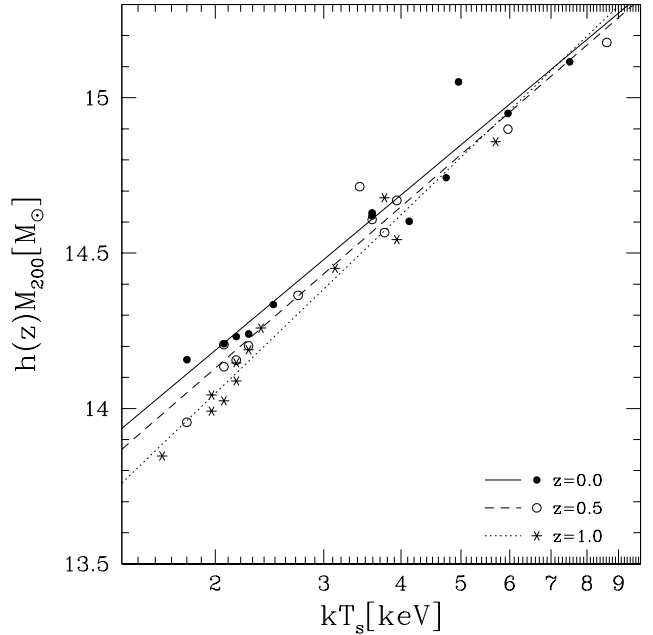


FIG. 12.— Redshift-corrected total mass within r_{200} vs. spectral temperature for models in set S3.

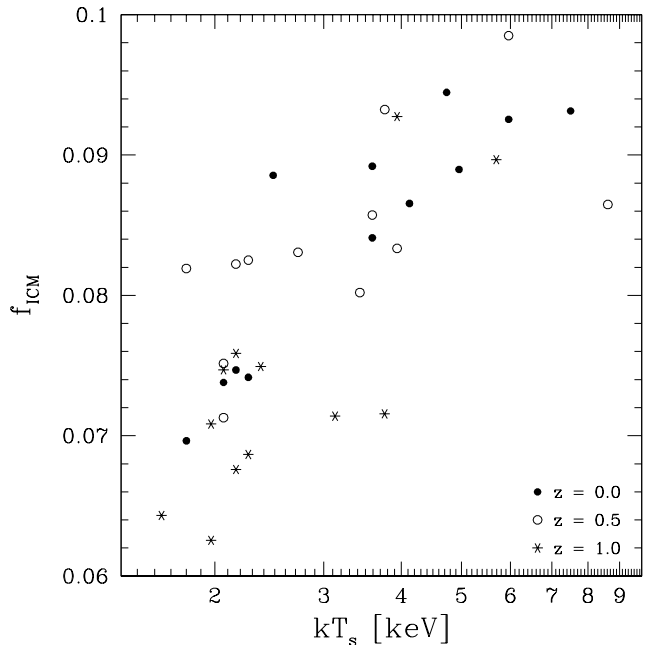


FIG. 13.— ICM mass as a fraction of total mass vs. spectral temperature inside r_{200} for clusters of model S3 at $z = 0.0, 0.5$ and 1.0 .

of the scaling relations at $z = 1.0$ which can be looked for in high redshift cluster observations coming from the current generation of X-ray satellites. These and deeper

TABLE 4

FITS^a TO THE R_I-T , L_X-T , $M_{ICM}-T$ RELATIONS FOR PREHEATING SET S3 ($h = 0.8$)

z	$M_{ICM}-T$		L_X-T		R_I-T	
	m	b	m	b	m	b
0.0	1.90(0.07)	13.83(0.02)	2.67(0.25)	44.89(0.07)	0.96(0.06)	-0.092(0.02)
0.5	1.97(0.09)	13.62(0.03)	2.59(0.25)	44.81(0.08)	0.93(0.09)	-0.13(0.03)
1.0	2.43(0.23)	13.49(0.08)	3.25(0.43)	44.85(0.15)	1.09(0.12)	-0.13(0.04)

^a Using the form $\log(X) = m \log(T_s/6 \text{ keV}) + b$.

observations may reveal the epoch where this model breaks down.

Without modeling the numerically complex processes which are thought to be responsible for preheating, we have produced simulated clusters that agree well with observation. Having shown preheating to be a viable solution to the long-standing discrepancies between theory and observation, there remains the task of delving deeper into the history of the ICM. One would like to know in detail the events which lead to a heated ICM. This simplified model cleanly produces clusters whose properties are consistent with observations of nearby clusters; the impending analysis of high redshift cluster observations from Chandra and XMM-Newton will guide us in building more detailed the-

oretical models of of the ICM's infancy.

The simulations were done, in part, using the computing facilities at the University of Michigan's Center for Parallel Computing. Our data processing was improved using `mekal`. JJB would like to thank Ben Mathiesen and Martin Sulkanen for their help with the spectral models. This work was supported by NASA through grant NAG5-7108 and NSF through grant AST-9803199. JJM is supported by Chandra Fellowship grant PF8-1003, awarded through the Chandra Science Center. The Chandra Science Center is operated by the Smithsonian Astrophysical Observatory for NASA under contract NAS8-39073.

APPENDIX

Let M_{Δ_c} be the total mass contained in a sphere (of radius r_{Δ_c} about the center) that encompasses a mean density $\Delta_c \rho_c$, where $\rho_c(z) \equiv 3H(z)^2/8\pi G$ is the critical density and $H(z)$ the Hubble parameter of the universe at epoch z . Write the ICM density $\rho_{ICM}(r)$ in terms of the natural radial variable $y \equiv r/r_{\Delta_c}$, structure function $g(y)$, and the ICM gas fraction within r_{Δ_c} , as in eqn's (2) and (3).

Clusters have no well-defined edge, but their hydrostatic regions are reasonably well bounded by r_{200} . We normalize the total cluster luminosity to be that interior to this radius

$$L_X = 4\pi \int_0^{r_{200}} dr r^2 n_e(r) n_H(r) \Lambda(T(r)) \quad (1)$$

where $\Lambda(T(r))$ is an appropriately normalized emissivity dependent only on temperature and $n_e = \rho_{ICM}/\mu_e m_p$ and $n_H = \rho_{ICM}/\mu_H m_p$ are the number densities of free electrons and protons. Assuming that the ICM is isothermal, we can define a dimensionless emissivity $\tilde{\Lambda}(T) \equiv \Lambda(T)/\Lambda(10 \text{ keV})$ by arbitrarily normalizing to emission at $T = 10$ keV. Using equations (2) and (3), the luminosity can be rewritten as

$$L_X \equiv C_X f_{ICM}^2 Q_L \tilde{\Lambda}(T) T^{\alpha_m} \quad (2)$$

where C_X carries dimension and depends only on fundamental constants and $Q_L = 3 \int_0^1 dy y^2 g^2(y)$. Note that Q_L is equivalent to the clumping factor $\langle \rho_{ICM}^2 \rangle / \langle \rho_{ICM} \rangle^2$, where the angle brackets denote the volume average over the cluster atmosphere. It is thus a structure factor which depends solely on the gas density shape and characterizes the concentration of the gas distribution.

Allowing expectations for f_{ICM} and Q_L to vary with cluster temperature produces eq. (8). To see the origin of the luminosity's canonical infall model temperature dependence, a set of additional assumptions are traditionally made: (i) pure bremsstrahlung emission ($\Lambda(T) \propto T^{1/2}$), (ii) virial equilibrium ($M_{200} \propto T^{3/2}$), (iii) structurally identical clusters ($Q_L(T) = C_1$) and (iv) constant gas fraction ($f_{ICM} = C_2$). This leads to the expected scaling relation between luminosity and temperature: $L_X \propto T^2$.

The scaling for the R_I-T relation is outlined in Mohr et al. (2000). Assuming no emission beyond r_{200} , then the surface brightness at r_{200} is formally zero. Consider the surface brightness at radius ξr_{200} where ξ is near, but below, unity

$$\Sigma(\xi r_{200}) = \frac{1}{2\pi(1+z)^4} \int_{-r_{200}\sqrt{1-\xi^2}}^{r_{200}\sqrt{1-\xi^2}} dl n_e(r) n_H(r) \Lambda(T) \quad (3)$$

where $r = \sqrt{(\xi r_{200})^2 + l^2}$. Rewriting using dimensionless variables as in the luminosity case above, we find

$$\Sigma(\xi r_{200}) = C_I f_{ICM}^2 Q_I \tilde{\Lambda}(T) T^{\alpha_m/3} \quad (4)$$

where C_I is a constant and $Q_I = \int_0^{\sqrt{1-\xi^2}} d\eta g^2(\sqrt{\eta^2 + \xi^2})$.

Assume that the β -model (Cavaliere & Fusco-Femiano 1976) describes the surface brightness profile

$$\Sigma(R) = \Sigma_0 \left(1 + \left(\frac{R}{R_c} \right)^2 \right)^{-3\beta + \frac{1}{2}} \quad (5)$$

Outside the core, the surface brightness scales as a power law in radius $\Sigma(R) \propto R^{-6\beta+1}$. In this regime, the surface brightness at an isophotal distance, $\Sigma(R_I)$, can be related to the surface brightness at radius ξr_{200}

$$R_I = \xi r_{200} \left(\frac{\Sigma(\xi r_{200})}{\Sigma(R_I)} \right)^{1/(6\beta-1)} \quad (6)$$

This adds a constraint on the shape parameter $Q_I \propto \xi^{1-6\beta}$. Using eq. (4) and introducing temperature dependence in f_{ICM} and Q_I then leads to the result eq. (9) of §3.1. For a typical observed value of $\beta = 2/3$ along with canonical assumptions for the other parameters, the predicted size temperature relation is $R_I \propto T^{2/3}$.

REFERENCES

- Allen S.W. & Fabian A.C., 1998, MNRAS, 297, L57.
 Arnaud M. & Evrard A.E., 1999, MNRAS, 305, 631
 Balogh M.L., Babul A., Patton D.R., 1999, MNRAS, 307, 463
 Barger A.J., Cowie L.L. & Richards E.A., 2000, ApJ, 119, 2092
 Baugh C.M., Cole S. & Frenk C.S., 1996, MNRAS, 283, 1361
 Blumenthal G.R., Faber S.M., Primack J.R., Rees M.J., 1984, Nature, 311, 517
 Blanchard A., Valls-Gabaud D. & Mamon G.A., 1992, A&A, 264, 365
 Bond J.R. & Efstathiou, 1984, ApJ, 285, L45
 Bower R.G., Benson A.J., Baugh C.M., Cole S., Frenk C.S., Lacey C.G., 2000, MNRAS, submitted, astro-ph/0006109
 Castander F.J. & Couch W.J., 1994, MNRAS, 268, 345
 Bower R.G., Lucey, J.R., & Ellis R.S., 1991, MNRAS, 254, 601
 Bryan, G.L. & Norman, M.L. 1998, ApJ, 495, 80.
 Cavaliere A., Menci N. & Tozzi P., 1999, MNRAS, 308, 599
 Cayatte V., Kotanyi C., Balkowski C. & van Gorkom J.H., 1994, ApJ, 107, 1003
 Chamaraux P., Balkowski C. & Gérard E., 1980, A&A, 83, 38
 Cole S., 1991, ApJ, 367, 45
 David L.P., Forman W. & Jones C., 1991, ApJ, 369, 121
 David L.P., Slyz A., Jones C., Forman W., Vrtillek S.D. & Arnaud K.A., 1993, ApJ, 412, 479
 Edge A.C. & Stewart G.C., 1991, MNRAS, 252, 414
 Edge A.C., Stewart G.C., Fabian A.C. & Arnaud K.A., 1990, MNRAS, 245, 559
 Efstathiou G., Davis M., Frenk C.S. & White S.D.M., 1985, ApJS, 57, 241.
 Eke V.R., Navarro J.F. & Frenk C.S., 1998, ApJ, 503, 569
 Evrard A.E., 1988, MNRAS, 235, 911
 Evrard A.E. & Henry J.P., 1991, ApJ, 383, 95
 Fabian A.C., Crawford C.S., Edge A.C. & Mushotzky R.F., 1994, MNRAS, 267, 779
 Fairley B.W., Jones L.R., Scharf C., Ebeling H., Perlman E., Horner D., Wegner G. & Malkan M., 2000, MNRAS, 315, 669
 Finoguenov A., Reiprich T.H. & Böhringer H., 2000, A&A, submitted, astro-ph/0010190
 Frenk C.S., White S.D.M., Bode P., Bond J.R., Bryan G.L., Cen R., Couchman H.M.P., Evrard A.E., Gnedin N., Jenkins A., Khokhlov A.M., Klypin A., Navarro J.F., Norman M.L., Ostriker J.P., Owen J.M., Pearce F.R., Pen U.-L., Steinmetz M., Thomas P.A., Villumsen J.V., Wadsley J.W., Warren M.S., Xu G., Yepes G., 1999, ApJ, 525, 554
 Gunn K.F. & Thomas P.A., 1996, MNRAS, 281, 1133
 Haiman Z., Mohr J.J. & Holden G.P., 2000, ApJ, submitted, astro-ph/0002336
 Hjorth J., Oukbir J. & van Kampen E., 1998, MNRAS, 298, L1
 Holder G.P., Mohr J.J., Carlstrom J.E., Evrard A.E. & Leitch E.M., 2000, ApJ, submitted, astro-ph/9912364
 Horner D.J., Mushotzky R.F. & Scharf C.A., 1999, ApJ, 520, 78
 Jing Y.P. & Suto Y., 2000, ApJ, 529, L69
 Jones, C & Forman W., 1984, ApJ, 276, 38
 Kaiser N., 1986, MNRAS, 222, 323
 Kaiser N., 1991, ApJ, 383, 104
 Kauffmann G., White S.D.M. & Guiderdoni B., 1993, MNRAS, 264, 201
 Kuntschner H., 2000, MNRAS, 315, 184
 Lloyd-Davies E.J., Ponman T.J., Cannon D.B., 2000, MNRAS, submitted, astro-ph/0002082
 Markevitch M., 1998, ApJ, 504, 27
 Mathiesen B. & Evrard A.E., 2001, ApJ, submitted, astro-ph/0004309
 Mathiesen B., Evrard A.E., Mohr J.J., 1999, ApJ, 520, L21
 Matsumoto H., Tsuru, T.G., Fukazawa Y., Hattori M. & Davis D.S., 2000, PASJ, 52, 153
 McNamara B.R., Wise M., Nulsen P.E.J., David L.P., Sarazin C.L., Bautz M., Markevitch M., Vikhlinin A., Forman W.R., Jones C. & Harris D.E., 2000, ApJ, 534, L135
 Metzler C.A., 1995, Ph.D. Thesis
 Metzler C.A. & Evrard A.E., 1997, astro-ph/9710324
 Metzler C.A., White M., Norman M. & Loken C., 1999, ApJ, 520, L9
 Mohr J.J. & Evrard A.E., 1997, ApJ, 491, 38
 Mohr J.J., Mathiesen B. & Evrard A.E., 1999, ApJ, 517, 627
 Mohr J.J., Reese E.D., Ellington E., Lewis A.D., Evrard A.E., 2000, ApJ, submitted, astro-ph/0004242
 Mushotzky R.F. & Scharf C.A., 1997, ApJ, 482, L13
 Nagai D., Sulkanen M.E. & Evrard A.E., 2000, MNRAS, 316, 120
 Navarro J.F., Frenk C.S., White S.D.M., 1995, MNRAS, 275, 720
 Neumann D.M. and Arnaud M., 1999, A&A, 348, 711
 Nevalainen J., Markevitch M., Forman W., 1999, ApJ, 528, 1
 Nevalainen J., Markevitch M., Forman W., 2000, ApJ, 532, 694
 Owen F., 2000, IAUJD, 10, 7
 Peebles P.J.E., 1982, ApJ, 263, L1
 Pen, U.-L., 1999, ApJ, 510, L1
 Pierre M., Bryan G., Gastaud R., 2000, A&A, 356, 403
 Rees M.J. & Ostriker J.P., 1977, MNRAS, 179, 541
 Roettiger K., Burns J.O. & Loken C., 1996, ApJ, 473, 651
 Somerville R.S., Primack J.R., 1999, MNRAS, 310, 1087
 Steidel C.C., Adelberger K.L., Giavalisco M., Dickinson M. & Pettini M., 1999, ApJ, 519, 1
 Thomas P.A., Muanwong O., Pearce F.R., Couchman H.M.P., Edge A.C., Jenkins A. & Onuora L., 2000, MNRAS, submitted, astro-ph/0007348
 Tozzi P. and Norman C., 2000, ApJ, submitted, astro-ph/0003289
 Trager S.C., Faber S.M., Worthey G. & González J.J., 2000, ApJ, 120, 165
 Van Dokkum P.G., Franx M., Fabricant D., Kelson D.D. & Illingworth G.D., 1999, ApJ, 520, L95
 White R.E., 1991, ApJ, 367, 69
 White S.D.M. & Frenk C.S., 1991, ApJ, 379, 52
 White S.D.M. & Rees M.J., 1978, MNRAS, 183, 341
 Wu K.K.S., Fabian A.C., Nulsen P.E.J., 1998, MNRAS, 301, L20
 Wu K.K.S., Fabian A.C., Nulsen P.E.J., 1999a, MNRAS, submitted, astro-ph/9907112
 Wu K.K.S., Fabian A.C., Nulsen P.E.J., 1999b, MNRAS, submitted, astro-ph/9910122
 XSPEC User's Manual:
<http://legacy.gsfc.nasa.gov/docs/xanadu/xspec/index.html>

TABLE 2
 CLUSTER PROPERTIES ($\Delta_c = 200, z = 0$)

Model	L ^a	M_{tot} ^b	M_{ICM} ^c	Υ	σ_{DM} ^d	T_m ^e	T_s ^f	$L_{X,bol}$ ^g	R_I ^h
a1S6	72.53	8.48	7.02	0.828	-85	5.72	6.24	2.89	0.5133
a2S6	72.53	3.01	1.88	0.625	-303	3.06	2.99	0.209	-
a31S6	53.34	3.90	2.54	0.651	-18	3.69	3.94	0.480	0.1937
a34S6	42.86	1.76	0.872	0.495	-91	2.23	2.48	0.0838	-
a190S6	37.89	1.37	0.395	0.288	-117	1.89	2.07	0.0193	-
a260S6	31.04	0.896	0.318	0.355	-30	1.52	1.80	0.0255	-
b1S6	82.43	10.4	8.80	0.846	-311	6.41	5.96	2.14	0.4246
b2S6	86.26	11.7	10.4	0.889	84	7.81	8.23	4.16	-
b31S6	51.56	5.31	3.31	0.623	-208	4.43	4.96	1.35	0.1937
b34S6	48.23	3.52	1.82	0.517	-157	3.35	3.59	0.244	-
b233S6	40.91	1.48	0.485	0.328	-53	2.06	2.27	0.0286	-
b255S6	32.99	1.30	0.493	0.379	-67	1.85	2.16	0.0443	-
a1S5	72.53	8.96	7.89	0.881	-51	5.91	6.24	4.30	0.5525
a2S5	72.53	3.58	2.66	0.743	-331	3.10	3.13	0.455	0.1309
a31S5	53.34	4.17	3.35	0.803	-37	3.65	3.94	0.987	0.3502
a34S5	42.86	1.95	1.41	0.723	-80	2.27	2.48	0.241	0.1489
a190S5	37.89	1.43	0.655	0.458	-61	1.85	2.16	0.0625	-
a260S5	31.04	0.952	0.497	0.522	-91	1.48	1.72	0.0672	0.0547
b1S5	82.43	11.4	10.2	0.895	-316	6.23	5.44	2.91	0.5074
b2S5	86.26	12.1	11.4	0.942	69	7.65	7.50	5.24	0.6496
b31S5	51.56	5.38	4.34	0.807	-22	4.69	5.19	3.95	0.4268
b34S5	48.23	3.74	2.73	0.730	-62	3.58	3.94	0.811	0.3261
b233S5	40.91	1.58	0.775	0.491	-87	1.99	2.27	0.0817	-
b255S5	32.99	1.41	0.753	0.534	-52	1.85	2.16	0.123	0.1146
a1S4	72.53	8.88	8.08	0.910	-74	5.79	5.96	4.97	0.5523
a2S4	72.53	3.70	2.96	0.800	-343	2.93	2.99	0.574	0.2287
a31S4	53.34	4.34	3.75	0.864	-63	3.57	3.94	1.40	0.4004
a34S4	42.86	2.06	1.76	0.854	-50	2.36	2.48	0.421	0.2540
a190S4	37.89	1.50	0.944	0.629	-64	1.79	2.07	0.145	0.1062
a260S4	31.04	1.23	0.760	0.618	-188	1.46	1.72	0.156	0.1529
b1S4	82.43	11.5	10.2	0.887	-309	5.96	5.19	3.13	0.5173
b2S4	86.26	13.0	12.1	0.931	130	7.76	7.50	7.02	0.6726
b31S4	51.56	5.46	4.93	0.903	30	4.75	4.96	6.20	0.4574
b34S4	48.23	3.98	3.29	0.827	-17	3.70	3.94	1.33	0.3973
b233S4	40.91	1.65	1.07	0.648	-86	1.93	2.16	0.177	0.1162
b255S4	32.99	1.62	1.05	0.648	-87	1.84	2.07	0.260	0.2038
a1S3	72.53	8.88	8.24	0.928	-53	5.80	5.96	5.37	0.5516
a2S3	72.53	2.51	3.50	0.839	-216	3.35	3.59	1.05	0.3965
a31S3	53.34	2.72	3.80	0.892	-40	3.41	3.59	1.41	0.4164
a34S3	42.86	1.37	1.91	0.884	-71	3.40	2.48	0.555	0.2856
a190S3	37.89	0.853	1.19	0.735	-71	1.83	2.07	0.257	0.1984
a260S3	31.04	0.716	1.00	0.694	-174	1.59	1.80	0.306	0.2064
b1S3	82.43	7.16	10.0	0.893	-300	5.81	4.96	3.26	0.5367
b2S3	86.26	8.70	12.2	0.938	110	7.81	7.50	8.24	0.6811
b31S3	51.56	3.74	5.22	0.944	116	4.69	4.73	6.55	0.4767
b34S3	48.23	2.48	3.46	0.865	41	3.76	4.12	1.79	0.4148
b233S3	40.91	0.922	1.29	0.741	-42	1.98	2.27	0.299	0.2148
b255S3	32.99	0.910	1.27	0.747	-13	1.94	2.16	0.445	0.2467
a1S2	72.53	8.88	8.32	0.937	-78	5.71	5.96	5.46	0.5591
a2S2	72.53	3.75	3.18	0.848	-369	2.79	2.72	0.685	0.2880
a31S2	53.34	4.29	3.80	0.886	-39	3.43	3.59	1.61	0.4192
a34S2	42.86	2.05	1.82	0.888	-68	2.28	2.37	0.508	0.2761
a190S2	37.89	1.59	1.26	0.792	-87	1.82	2.07	0.303	0.2289
a260S2	31.04	1.50	1.12	0.747	-158	1.65	1.88	0.471	0.2234
b1S2	82.43	11.1	9.84	0.886	-293	5.72	4.96	3.21	0.5472
b2S2	86.26	13.0	12.2	0.938	104	7.79	7.50	9.02	0.6827

TABLE 2—*Continued*

Model	L^a	M_{tot}^b	M_{ICM}^c	Υ	σ_{DM}^d	T_m^e	T_s^f	$L_{X,bot}^g$	R_I^h
b31S2	51.56	5.62	5.30	0.943	108	4.61	4.52	0.637	0.4794
b34S2	48.23	4.09	3.55	0.868	28	3.77	4.12	1.95	0.4257
b233S2	40.91	1.72	1.53	0.890	-83	1.90	2.16	0.335	0.2309
b255S2	32.99	1.74	1.37	0.787	5	1.99	2.16	0.593	0.2597
a1S1	72.53	8.82	8.24	0.934	-47	5.73	5.69	6.20	0.6038
a2S1	72.53	2.44	2.04	0.836	-196	2.21	2.27	0.415	0.2888
a31S1	53.34	4.42	3.87	0.876	-18	3.50	3.59	1.84	0.4522
a34S1	42.86	2.10	1.94	0.924	-41	2.24	2.37	0.806	0.3224
a190S1	37.89	1.71	1.49	0.871	-53	1.90	2.16	0.529	0.2904
a260S1	31.04	1.59	1.36	0.855	-152	1.72	1.88	0.922	0.2648
b1S1	82.43	11.2	9.60	0.857	-257	5.63	4.96	3.46	0.6049
b2S1	86.26	13.4	12.5	0.933	92	7.80	7.50	10.4	0.7737
b31S1	51.56	5.84	5.48	0.938	143	4.57	4.32	7.17	0.5180
b34S1	48.23	3.98	3.52	0.884	-81	3.64	4.12	2.48	0.4508
b233S1	40.91	1.74	1.52	0.874	-7	1.96	2.16	0.540	0.3194
b255S1	32.99	1.78	1.54	0.865	2	2.01	2.16	0.928	0.2985
a1S0	72.53	8.96	8.32	0.929	-72	5.55	5.19	7.87	0.5561
a2S0	72.53	3.41	2.81	0.824	-308	2.52	2.48	0.806	0.3349
a31S0	53.34	4.40	3.84	0.873	-26	3.28	3.28	2.34	0.4179
a34S0	42.86	2.11	1.93	0.915	-73	2.13	2.07	1.32	0.3081
a190S0	37.89	1.86	1.66	0.892	5	1.95	2.07	0.922	0.2846
a260S0	31.04	1.75	1.55	0.886	-136	1.53	1.64	2.59	0.2997
b1S0	82.43	10.7	9.12	0.852	-202	5.44	4.32	3.75	0.5665
b2S0	86.26	13.6	12.6	0.926	-77	7.73	7.17	14.3	0.6556
b31S0	51.56	5.95	5.41	0.909	147	4.19	3.42	7.87	0.4795
b34S0	48.23	4.06	3.58	0.882	-42	3.59	3.59	3.47	0.4069
b233S0	40.91	1.80	1.59	0.883	18	1.94	2.07	0.992	0.2925
b255S0	32.99	1.92	1.64	0.854	3	1.85	1.80	1.97	0.2794

^a[h^{-1} Mpc]^b[$h^{-1} 10^{14} M_{\odot}$]^c[$h^{-1} 10^{13} M_{\odot}$]^d[km/s]^e[K]^f[K]^g[$h^{-2} 10^{44}$ erg/s]^h[h^{-1} Mpc], dashed entries result from no emission above the chosen isophote

FIG. 6.— X-ray surface-brightness (SB) images for cluster a1 both non-preheated (S0, left), moderately preheated (S3, middle) and excessively preheated (S6, right) at four redshifts (0.0, bottom; 0.5; 1.0; 2.0, top).

FIG. 7.— X-ray temperature maps for cluster a1 both non-preheated (S0, left), moderately preheated (S3, middle) and excessively preheated (S6, right) at four redshifts (0.0, bottom; 0.5; 1.0; 2.0, top).

FIG. 8.— Sunyaev-Zel'dovich effect (SZ) X-ray images for cluster a1 both non-preheated (S0, left), moderately preheated (S3, middle) and excessively preheated (S6, right) at four redshifts (0.0, bottom; 0.5; 1.0; 2.0, top).

This figure "figure6.gif" is available in "gif" format from:

<http://arxiv.org/ps/astro-ph/0010584v1>

This figure "figure7.gif" is available in "gif" format from:

<http://arxiv.org/ps/astro-ph/0010584v1>

This figure "figure8.gif" is available in "gif" format from:

<http://arxiv.org/ps/astro-ph/0010584v1>